

Atomic structure of metal-halide perovskites from first principles: The chicken-and-egg paradox of the organic-inorganic interaction

Jingrui Li* and Patrick Rinke

Centre of Excellence in Computational Nanoscience (COMP) and Department of Applied Physics,
Aalto University, P.O.Box 11100, FI-00076 AALTO, Finland

We have studied the prototype hybrid organic-inorganic perovskite $\text{CH}_3\text{NH}_3\text{PbI}_3$ and its three close relatives, $\text{CH}_3\text{NH}_3\text{SnI}_3$, $\text{CH}_3\text{NH}_3\text{PbCl}_3$ and CsPbI_3 , using relativistic density function theory. The long-range van der Waals (vdW) interactions were incorporated into the Perdew-Burke-Ernzerhof (PBE) exchange-correlation functional using the Tkatchenko-Scheffler pairwise scheme. Our results reveal that hydrogen bonding, which is well described by the PBE functional, plays a decisive role for the structural parameters of these systems, including the position and orientation of the organic cation as well as the deformation of the inorganic framework. The magnitude of the inorganic-framework deformation depends sensitively on the orientation of the organic cation, and directly influences the stability of the hybrid perovskites. Our results suggest that the organic and the inorganic components complement each other: The low symmetry of the organic cation is the origin of the inorganic-framework deformation, which then aids the overall stabilization of the hybrid perovskite structure. This stabilization is indirectly affected by vdW interactions, which lead to smaller unit-cell volumes than in PBE and therefore modulate the interaction between the organic cation and the inorganic framework. The vdW-induced lattice-constant corrections are system dependent and lead to PBE+vdW lattice constants in good agreement with experiment. Further insight is gained by analysing the vdW contributions. In all iodide-based hybrid perovskites the interaction between the organic cation and the iodide anions provides the largest lattice-constant change, followed by iodine-iodine and the organic cation – heavy-metal cation interaction. These corrections follow an almost linear dependence on the lattice constant within the range considered in our study, and are therefore approximately additive.

I. INTRODUCTION

Hybrid perovskite photovoltaics (HPPV)^{1,2} has surprised the photovoltaic community with its record increase in power-conversion efficiency (PCE) during the last three years³. The photovoltaic utilization of hybrid organometal-halide perovskites, especially the prototype compound methylammonium ($\text{MA}^+ \equiv \text{CH}_3\text{NH}_3^+$) lead triiodide ($\text{CH}_3\text{NH}_3\text{PbI}_3$, shortened as MAPbI_3 hereafter), was pioneered by Kojima *et al.*, who used these materials as sensitizers in dye-sensitized solar cells and obtained 3.8% PCE⁴. The current state-of-the-art HPPV architecture was proposed in 2012 by replacing the liquid electrolyte with solid-state hole-transporting materials, achieving $\sim 10\%$ PCE^{5,6}. This triggered a rapid PCE improvement, as reflected by the current PCE record of HPPVs that broke the 20% mark⁷. This PCE is already quite close to the best performing inorganic-based single-junction thin-film cells, such as CdTe. As photoactive materials, hybrid perovskites show several essential advantages in photovoltaic applications, such as band gaps close to the optimal value for single-junction solar-cell absorbers⁸, excellent absorption properties in the visible part of the solar spectrum⁹, and high mobilities for both electron and hole transport^{10,11}, as well as low-temperature processing, low manufacturing cost, light weight, and environmental friendliness. Therefore, HPPVs have become promising candidates for solar-cell devices which can offer clean, affordable and sustainable energy.

Theoretical investigations play an important role in understanding the materials properties and fundamental processes for emergent solar-cell research. Along with the rapid development of HPPV technologies, various theoretical studies have been carried out for hybrid-perovskite-based systems in recent years^{12–16}. Interesting aspects of these

studies include the crystal structures of hybrid perovskites in different phases^{17–20}, the importance of spin-orbit coupling (SOC)^{21–24}, many-body effects^{23,25,26}, and ferroelectric effects for the electronic structure of hybrid-perovskite semiconductors^{27–29}. However, many challenges remain despite this recent progress. For example, the atomic structure of these materials is still riddled with controversies and it is not yet clear which theoretical approach is most suitable. This is a fundamental question in computational materials science and a prerequisite for further theoretical investigations, especially due to the extreme complexity in the structure of hybrid perovskites. In this context, Brivio *et al.* observed three local total-energy minima associated with different MA^+ -orientations in MAPbI_3 ¹³, for which Frost *et al.* obtained a distribution using *ab initio* molecular dynamics, claiming that the orientation of C–N bonds along the [100] direction (“face-to-face”) is the most populated²⁸. Egger and Kronik found only one preferred MA^+ -orientation and attributed its stability to hydrogen bonding³⁰. Motta *et al.* reported two local total-energy minima with a ~ 20 meV-per-unit-cell difference in favor of the “[011]”-orientation which is very close to the structure studied by Egger and Kronik but very different from the “[110]” (“edge-to-edge”) structure of Brivio *et al.*³¹. Conversely, the calculations by Yin *et al.* indicated that the “[111]”-orientation (along the diagonal of the unit cell) is energetically more favorable¹⁶. This plethora of competing structural models is a result of different computational approaches, for example, different density functionals, the use of the long-range van der Waals (vdW) interactions, and full relativistic effects.

In this work, we perform a comprehensive analysis of the atomic structure of hybrid perovskites. We focus on the impact of dispersive interactions, which have only been included

in three of the many density-functional-theory (DFT) calculations for HPPVs^{30–32}. It was shown that the incorporation of vdW interactions into the DFT calculations results in unit-cell volumes in good agreement with experiments. However, the impact of vdW interactions on the atomic structure (including the relative location of the organic cation and the deformation of the inorganic framework) has not been investigated so far. Employing the Tkatchenko-Scheffler (TS) pairwise dispersion scheme³³, Egger and Kronik were able to calculate the vdW interaction energy between each interatomic pair for an optimized MAPbI_3 geometry, and found that the iodine-iodine interaction (~ 100 meV per pair) has the largest contribution to the overall dispersive (TS) correction of total energy³⁰. Nevertheless, more calculations and analysis are required to understand the impact of vdW interactions on the atomic structure of hybrid perovskites.

In this work, we investigated the prototype hybrid perovskite MAPbI_3 and three isostructural systems, methylammonium tin triiodide (MASnI_3), methylammonium lead trichloride (MAPbCl_3) and caesium lead triiodide (CsPbI_3). These three perovskites can be regarded as close relatives of the prototype $\text{MA}_1^{(I)}\text{Pb}_1^{(II)}\text{I}_3^{(-I)}$, as each of them only differs from it by one component: the monovalent cation (CsPbI_3), the divalent cation (MASnI_3), or the halide (MAPbCl_3). Thus, our study facilitates a systematic analysis of interatomic interactions in metal- and organometal-trihalide perovskites. For example, we can compare the vdW interactions between the organic MA^+ cation and the iodide anions in MAPbI_3 and in MASnI_3 , or the MA-I interaction in MAPbI_3 and its counterpart (Cs-I) in CsPbI_3 .

Of particular interest in this paper is the question how the organic and the inorganic component in HPPVs interact with each other. Does the inorganic framework deform on its own and the MA^+ cation then accommodates itself in a particular orientation in the deformed cage? Or does the MA^+ cation force the inorganic framework into a particular deformation? We address this *chicken-and-egg* problem with density-functional theory to gain atomistic insight that will be useful for future HPPV design. In addition, we ask the question: which effect vdW interactions and hydrogen bonds have on the interplay between the organic and the inorganic component in HPPVs?

The remainder of this paper is organized as follows: In Section II we outline the model systems and the computational details of our DFT calculations. Section III presents the lattice constants and atomic structures for all considered systems. We discuss the interplay of the organic cation and the inorganic framework as well as the impact of vdW interactions in detail. Finally, Section IV concludes with a summary.

II. MODELS AND COMPUTATIONAL DETAILS

We adopted the cubic ($\text{Pm}\bar{3}\text{m}$) primitive-cell model for all compounds thus neglecting the disorder of MA^+ cations. The ions were initially placed at the Wyckoff positions of the $\text{Pm}\bar{3}\text{m}$ space group, as shown in Fig. 1: the monovalent cation $\text{A}^+ = \text{MA}^+$ or Cs^+ at 1b, the divalent heavy-

metal cation $\text{B}^{2+} = \text{Pb}^{2+}$ or Sn^{2+} at 1a, and the halide anions $\text{X}^- = \text{I}^-$ or Cl^- at 3d. For hybrid (organic-inorganic) perovskites, the organic MA^+ cation was initially placed at the unit-cell center (the 1b Wyckoff position) with several inequivalent C-N orientations. This model not only allows for a direct comparison to previous studies, but can also provide a basic and informative description of the atomic structure. We are currently also carrying out first-principles calculations for supercell models. The results will be presented elsewhere in the future.

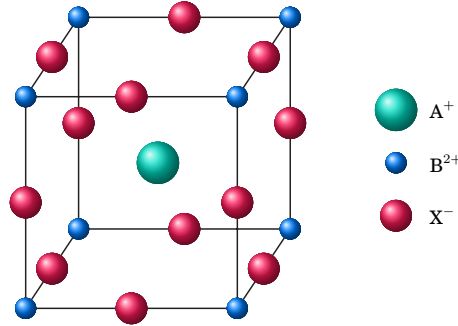


Figure 1. Cubic primitive cell of the perovskite structure used to model the investigated compounds ABX_3 in this paper. The monovalent cation A^+ , the divalent cation B^{2+} and the halide anions X^- are represented by the green, blue and red spheres, respectively.

For each perovskite, we optimized the lattice constant and atomic geometry using the following protocol: (i) The forces on the nuclei were minimized for a fixed shape and size of the cubic unit-cell. (ii) The optimized lattice constant was determined from the minimum of the total-energy *vs.* volume curve. We used the Perdew-Burke-Ernzerhof (PBE) generalized gradient approximation³⁴ as the exchange-correlation functional throughout this work. This choice was based on our test calculations, which indicated that hybrid functionals (that combine exact exchange with PBE exchange) change the lattice constants by less than 0.3%, but increase the computational cost (both memory and CPU time) by approximately one order of magnitude. SOC, which has already been demonstrated to be very important for the electronic structures of (especially lead-based) hybrid perovskites^{21–24}, does not strongly influence the lattice constants as shown by Egger *et al.*³⁰ and our test calculations. Thus, we only included scalar relativistic effects in our calculations via the zero-order regular approximation³⁵. Corrections due to long-range vdW interactions were taken into account by employing the TS method based on the Hirshfeld partitioning of the electron density³³. Accordingly, the calculations incorporating TS-vdW are labelled by “PBE+vdW” hereafter. We used the default parameters in TS-vdW for neutral atoms (listed in Table S1 of the Supplemental Material, SM) without explicitly calculating the C_6 coefficients based on ionic reference systems^{36–38}. A Γ -centered $8 \times 8 \times 8$ k-point mesh was used for the periodic DFT calculations. All calculations were performed using the all-electron local-atomic-orbital code FHI-aims^{39–41}.

III. RESULTS AND DISCUSSIONS

A. Lattice constants and orientations of the C–N bond in the optimized geometries

At each trial lattice constant, the optimization of our hybrid perovskites results in two local total-energy minima, corresponding to two different structures denoted by **MABX₃–a** and **b**, as illustrated in Fig. 2. For ease of reporting, we shift the whole lattice so that the coordinate of Pb²⁺ or Sn²⁺ becomes (0, 0, 0) (the 1a Wyckoff position). The two geometries correspond to two orientations of the C–N bond. In case **a**, the C–N bond is precisely oriented along the [111] (diagonal) direction and colinear with the unit-cell center as well as the Pb²⁺ or Sn²⁺ atom. In case **b**, the C–N bond is located in the (020) plane and deviates from the [100] (face-to-face) direction by an angle which depends on the hybrid-perovskite composition, the lattice constant, and the DFT method. For CsPbI₃, the structure remained in the initial cubic geometry during the relaxation.

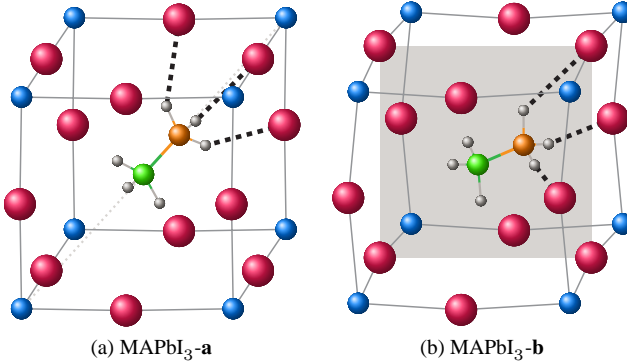


Figure 2. Cubic unit cell of MAPbI₃ optimized with PBE+vdW: (a) structure **a**, with the colinearity of Pb (blue), C (green) and N (orange) indicated by the gray dotted line; and (b) structure **b**, with indicating the (020) plane where the C–N bond is located in gray. The hydrogen bonds between I[–] anions (red) and H atoms (gray) in the $-\text{NH}_3^+$ group are highlighted by black dashed lines.

For a quantitative description of the atomic structure, we define several quantities that are related to the location of the organic cation and the deformation of the inorganic framework. The definition of these quantities is illustrated graphically in Fig. 3. The orientation of MA⁺ is characterized by $\Delta x : \Delta y : \Delta z(\text{C–N})$, the ratio among the projection of the C–N bond onto the lattice-vector directions x , y and z (Fig. 3a). The position of MA⁺ relative to the center of the cubic unit cell is described by u_{NC} , which is defined by the ratio of the nitrogen-to-cell-center distance to the carbon-to-cell-center distance (Fig. 3b). The $\Delta(X)$ values, that is, the deviation of an X[–] cation from its “ideal” Wyckoff position in the Pm $\bar{3}$ m space group (see Fig. 3c), is closely related to the deformation of the BX₃^{2–}-framework. Since we are working within the cubic primitive-cell model for all considered systems in this paper, we can use dimensionless fractional co-

ordinates to calculate distances.

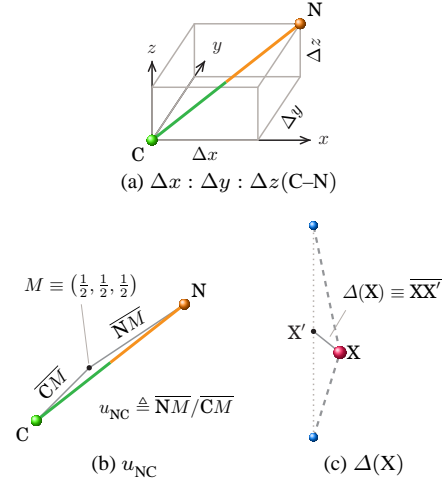


Figure 3. Graphical representation of observables defined to characterize the atomic structure of hybrid perovskites: (a) $\Delta x : \Delta y : \Delta z(\text{C–N})$, (b) u_{NC} and (c) $\Delta(X)$. The carbon, nitrogen, halide and divalent metal atoms are colored in green, orange, red and blue, respectively. In (a), Δx , Δy and Δz are the projections of the C–N bond onto the lattice-vector directions x , y and z , respectively. In (b), M denotes the unit-cell center, and NM and CM are the distances between it and the carbon and nitrogen atoms, respectively. u_{NC} is defined by their ratio. In (c), X' denotes the Wyckoff position for the X[–] anion, and $\Delta(X)$ is the distance between it and the position of X[–] in the real system.

The $\Delta x : \Delta y : \Delta z(\text{C–N})$ ratio in case **a** is 1 : 1 : 1 (or $-1 : 1 : 1$, and so forth, for other equivalent structures). In case **b**, this ratio can be written as $r : 0 : 1$ (or equivalently $-1 : r : 0$, and so forth) with $r > 1$. The angle between the C–N bond and the [100] direction is $\arctan(r^{-1})$.

Table I lists the results of our geometry optimization. First, for each hybrid perovskite, the lattice constant of case **a** is larger than case **b**, but the difference is small. Therefore, different orientations of the C–N bond do not cause large changes in the unit-cell volume in this cubic primitive-cell model. Second, the inclusion of TS-vdW causes a significant reduction of the optimized lattice constants (approximately 2.0%, 2.6%, 1.6% and 3.7% for MAPbI₃, MASnI₃, MAPbCl₃ and CsPbI₃, respectively). The lattice constants optimized with PBE+vdW agree well with experimental data. Specifically, for both MAPbI₃ and MASnI₃ the overestimation amounts to $\sim 0.6\%$, for MAPbCl₃ the overestimation is $\sim 1.1\%$, and for CsPbI₃ the underestimation is less than 0.2%. These lattice constants agree well with the first-principles studies of Egger *et al.*³⁰ and Motta *et al.*³¹. Third, structure **b** is more stable than **a** for all investigated hybrid compounds as it corresponds to a lower total-energy minimum. A larger total-energy difference (thus also cohesive-energy difference) is obtained when including TS-vdW in the PBE calculations.

We have also performed direct lattice-vector optimization using the analytical stress tensor implemented in FHI-aims⁴⁶. For case **a**, the optimized structure remains cubic with slight difference in the lattice constants; while

Table I. Results of the geometry optimization (using PBE and PBE+vdW) of the investigated perovskites (in both structures **a** and **b** for hybrid systems): lattice constant a of the cubic unit cell (compared with experimental results a_{exp}), orientation of C–N bond given by the $\Delta x : \Delta y : \Delta z$ (C–N) ratio (see Fig. 3a for definition), and the total-energy difference between structures **a** and **b**: $\Delta E_{\text{total}} \triangleq E_{\text{total}}(\mathbf{b}) - E_{\text{total}}(\mathbf{a})$. All lattice constants are in Å; all energies are in meV (per ABX_3 -unit, similarly hereinafter otherwise stated).

	structure a		structure b	
	PBE	PBE+vdW	PBE	PBE+vdW
MAPbI ₃ : $a_{\text{exp}} = 6.313$ (> 323 K) ⁴² , 6.329 (> 327 K) ⁴³				
a	6.491	6.364	6.486	6.350
$\Delta x : \Delta y : \Delta z$ (C–N)	1:1:1	1:1:1	4.434:0:1	2.330:0:1
ΔE_{total}	–	–	–10.5	–20.9
MASnI ₃ : $a_{\text{exp}} = 6.231$ (293 K) ⁴²				
a	6.454	6.268	6.410	6.257
$\Delta x : \Delta y : \Delta z$ (C–N)	1:1:1	1:1:1	3.901:0:1	2.313:0:1
ΔE_{total}	–	–	–3.3	–21.6
MAPbCl ₃ : $a_{\text{exp}} = 5.669$ (280 K) ⁴⁴				
a	5.843	5.745	5.811	5.717
$\Delta x : \Delta y : \Delta z$ (C–N)	1:1:1	1:1:1	3.289:0:1	2.483:0:1
ΔE_{total}	–	–	–7.7	–37.2
CsPbI ₃ : $a_{\text{exp}} = 6.177$ Å (> 583 K) ⁴⁵				
a	6.400	6.166	–	–

for case **b**, the cubic symmetry is broken, resulting in an orthorhombic lattice. To focus our analysis, we therefore do not further discuss the results of the stress-tensor optimization in this paper, but will return to it in future work.

Furthermore, we remark that caution has to be applied when comparing DFT lattice constants to experiment. Conventional DFT calculations (for example, the PBE+vdW calculations in this work) are carried out at 0 K, while experimental lattice constants for the cubic structures of hybrid perovskites are measured at room temperature or above. For example, the lattice constant 6.313 Å for MAPbI₃ was measured at above 50 °C⁴². The lattice constant at 323 K will therefore likely be larger than that at 0 K due to thermal expansion. Preliminary calculations indicate that the thermal expansion is of the order of 0.01 Å/100 K⁴⁷ and therefore will only change the lattice constant at 323 K by approximately 0.03 Å.

Table II lists the C–N bond length and the distance between each hydrogen atom in the ammonium group (H(N)) and the nearest halide anion for each optimized geometry. In all cases, the C–N bond length is ~1.49 Å, and other interatomic distances within the MA⁺ cation do not exhibit a pronounced dependence on the composition of the hybrid perovskite or the DFT method (data not shown).

The H(N)–X distances indicate typical hydrogen-bonding character for all MA-based compounds. For case **a**, all three distances are equal to each other, while for case **b** we obtained two different values. The H(N)–I distances in MABI₃-**a** and **b** lie between 2.65 and 2.81 Å. These values agree well with recent neutron powder diffraction data (2.61 – 2.81 Å) for MAPbI₃⁴⁸ and are close to the H–I distance (2.598 Å) in NH₄I measured by single

Table II. C–N bond length $\overline{\text{C–N}}$ and hydrogen-bond lengths $\text{H(N)} \cdots \text{X}$ (both in Å) in geometry-optimized perovskites (using PBE and PBE+vdW). Results for both cases **a** and **b** are shown.

	structure a		structure b	
	PBE	PBE+vdW	PBE	PBE+vdW
MAPbI ₃				
$\overline{\text{C–N}}$	1.492	1.490	1.492	1.492
$\text{H(N)} \cdots \text{I}$	2.679	2.681	2.656	2.695
			2.738	2.807
MASnI ₃				
$\overline{\text{C–N}}$	1.492	1.489	1.492	1.491
$\text{H(N)} \cdots \text{I}$	2.661	2.672	2.658	2.677
			2.719	2.783
MAPbCl ₃				
$\overline{\text{C–N}}$	1.487	1.485	1.488	1.487
$\text{H(N)} \cdots \text{Cl}$	2.273	2.284	2.305	2.310
			2.338	2.382

crystal neutron diffraction⁴⁹. They are also very close to the value of 2.65 Å obtained from a previous *ab initio* Car-Parrinello molecular dynamics study using PBE¹⁹. Similarly, the H(N)–Cl distances in MAPbCl₃ are very close to the value in NH₄Cl (2.32 ± 0.02 Å) obtained from neutron-diffraction experiments⁵⁰. This hydrogen-bonding character does not change appreciably when the TS-vdW interaction is not included. We have performed test calculations for

MAPbI₃-**a** in which we switched off the vdW interactions between H and I. The results show negligible changes in both lattice constant and hydrogen-bond lengths. This demonstrates that PBE describes hydrogen bonding well in hybrid perovskites, which is in line with previous PBE studies of hydrogen bonding⁵¹⁻⁵³.

For MA-based perovskites, structures **a** and **b** provide two obvious possibilities for all three hydrogen atoms in the -NH₃⁺ group to form hydrogen bonds with halide anions. Other orientations were considered in some previous theoretical works, for example, the [110] (edge-to-edge) orientation^{13,28}. This orientation is not suitable for hydrogen bonding, because all N-H bonds point toward face centers or cube corners thus being far away from the halide anions.

B. Atomic structure of the optimized geometries

We start our discussion of the atomic structure with case **a**. Table III lists some of the coordinates (please refer to Table S2 for the full data) as well as structural parameters u_{NC} and $\Delta(X)$.

Table III shows that all systems of structure **a** are strictly isotropic in three dimensions due to the rotational symmetry with respect to the three-fold axes along the [111] (diagonal, *cf.* Fig. 2a) direction. However, the organic cation and all three halide anions are not located at their ideal Wyckoff positions of the Pm $\bar{3}$ m space group. The center of MA⁺ deviates from the center of the cubic unit cell (the 1b Wyckoff position) so that the nitrogen-end is closer to the (1, 1, 1)-vertex, and the carbon-end moves toward ($\frac{1}{2}$, $\frac{1}{2}$, $\frac{1}{2}$) accordingly. Consequently, the three hydrogen atoms of the ammonium group are closer to the three halide anions whose positions are approximately ($\frac{1}{2}$, 1, 1), (1, $\frac{1}{2}$, 1) and (1, 1, $\frac{1}{2}$). This significantly favors the development of H(N)· · · X distances for hydrogen-bonding. We use the u_{NC} parameter (Fig. 3b) to characterize this displacement. Table III shows that, by including TS-vdW in the PBE calculations, the u_{NC} values of all hybrid perovskites decrease, indicating a smaller displacement of MA⁺ cation from the unit-cell center. This can be rationalized by simple geometrical considerations based on the H(N)· · · X distance and the unit-cell-volume reduction caused by the vdW interactions.

The halide anions in hybrid perovskites of structure **a** are “pulled” away from their ideal (3d Wyckoff) positions toward the nitrogen-end of the MA⁺ cation. This is reflected by the coordinates of the X⁻ anions and their $\Delta(X)$ values. Such a deformation of the inorganic framework is closely related to the formation of hydrogen bonds. For example, in the PBE geometry of MAPbI₃-**a**, the distance between the iodide anion at (0.487, 0.984, 0.984) and a hydrogen atom of the -NH₃⁺ group at (0.512, 0.693, 0.693) (*cf.* Table S2) is 2.679 Å, while the distance between this H atom and the corresponding 3d Wyckoff position ($\frac{1}{2}$, 1, 1) is 2.821 Å, being > 5% larger than the former value and unlikely appropriate for H · · · I hydrogen bonding. Table III reveals that all three inequivalent X⁻ anions equally participate in the hydrogen bonding. Therefore, the resulting deviation from their ideal locations exhibits

Table III. Fractional coordinates of the carbon and nitrogen atoms as well as all inequivalent halide anions in the optimized geometries (using PBE and PBE+vdW) of the investigated hybrid perovskites in structure **a**. Lead or tin atoms are located at (0, 0, 0). $\Delta(X)$ is the deviation of each halide anion from the ideal position: ($\frac{1}{2}$, 1, 1), (1, $\frac{1}{2}$, 1) or (1, 1, $\frac{1}{2}$). Also listed is the u_{NC} value for each system. All data are dimensionless.

	PBE				PBE+vdW			
	x	y	z	$\Delta(X)$	x	y	z	$\Delta(X)$
MAPbI₃								
C	0.464	0.464	0.464		0.462	0.462	0.462	
N	0.596	0.596	0.596		0.597	0.597	0.597	
u_{NC}			2.655				2.580	
I	0.487	0.984	0.984	0.026	0.496	0.993	0.994	0.010
I	0.984	0.487	0.984	0.026	0.994	0.496	0.993	0.010
I	0.984	0.984	0.487	0.026	0.993	0.994	0.496	0.010
MASnI₃								
C	0.461	0.461	0.461		0.452	0.452	0.452	
N	0.594	0.594	0.594		0.589	0.589	0.589	
u_{NC}			2.417				1.874	
I	0.466	0.981	0.981	0.043	0.489	0.991	0.991	0.017
I	0.981	0.466	0.981	0.043	0.991	0.489	0.991	0.017
I	0.981	0.981	0.466	0.043	0.991	0.991	0.489	0.017
MAPbCl₃								
C	0.452	0.452	0.452		0.443	0.443	0.443	
N	0.598	0.598	0.598		0.592	0.592	0.592	
u_{NC}			2.031				1.607	
Cl	0.484	0.981	0.981	0.032	0.492	0.982	0.982	0.026
Cl	0.981	0.484	0.981	0.032	0.982	0.492	0.982	0.026
Cl	0.981	0.981	0.484	0.032	0.982	0.982	0.492	0.026

a three-dimensional isotropic character. By incorporating TS-vdW into the DFT calculations, this deviation decreases noticeably especially for both iodide-based perovskites. The deformation of the BX₃²⁻-framework is very common in materials with perovskite structure. It can trigger several deviations from the ideal cubic structure, such as the distortion of the BX₆-octahedron, the off-center displacement of B in the octahedron, and the well-known octahedron-tilting^{17,42,44,54,55}. To model these features, we would need to go beyond the primitive-cell model in future studies.

From the PBE+vdW results of structure **a**, we observe an interesting correspondence between u_{NC} and $\Delta(X)$ among the three hybrid perovskites: As u_{NC} decreases from MAPbI₃, MASnI₃ to MAPbCl₃ (so does the lattice constant a), that is, the MA⁺ cation becomes closer to the unit-cell center, $\Delta(X)$ increases, indicating a larger magnitude of the inorganic-framework deformation. A graphical representation is given in Fig. 4.

Now we turn to structure **b**. Table IV lists the coordinates for carbon, nitrogen and halide atoms. We reiterate that there is an essential difference between the geometry of structure **a**

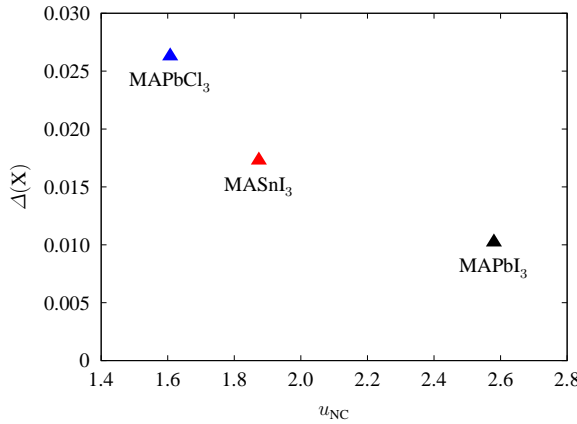


Figure 4. PBE+vdW results of u_{NC} and $\Delta(X)$ for $\text{MAPbI}_3\text{-a}$ (black), $\text{MASnI}_3\text{-a}$ (red) and $\text{MAPbCl}_3\text{-a}$ (blue).

and **b**: structure **b** does not show three-dimensional isotropy as structure **a**, instead it exhibits reflectional symmetry with respect to the (020) plane, in which the C–N bond is located (*cf.* Fig. 2b).

We first analyse the geometry of the organic MA^+ cation. This requires two observables: position and orientation. The position of MA^+ is described by the u_{NC} value characterizing its displacement from the unit-cell center (note: unlike in structure **a**, the unit-cell center is not colinear with the C–N bond in structure **b**). Table IV shows that, similar to structure **a**, u_{NC} decreases when TS-vdW is included in the DFT calculations, which corresponds to a smaller displacement of the MA^+ cation from $(\frac{1}{2}, \frac{1}{2}, \frac{1}{2})$. The C–N bond in structure **b** is located within the (020) plane (the xz plane that equally divides the unit cell) with an orientation characterized by the $\Delta x : \Delta y : \Delta z(\text{C–N})$ values listed in Table II. For each investigated system, the inclusion of TS-vdW results in a smaller $\Delta x : \Delta z$ ratio, that is, a larger angle between the C–N bond and the [100] (face-to-face) direction. For example, this angle is $\arctan(4.434^{-1}) = 12.3^\circ$ in the PBE geometry of MAPbI_3 , and becomes $\arctan(2.330^{-1}) = 23.2^\circ$ in the PBE+vdW geometry.

Similar to structure **a**, the position and orientation of MA^+ in structure **b** adjust to form hydrogen bonds between the hydrogen atoms at the nitrogen-end and the halide anions. Since there are two parameters determining the MA^+ -geometry, it is not easy to derive a clear trend among the three investigated hybrid perovskites. Nevertheless, we can still determine some relationships. For example, Table II shows very close $\Delta x : \Delta y : \Delta z(\text{C–N})$ ratios for the geometry of the two iodide-based hybrid perovskites optimized with PBE+vdW, while the lattice constant of $\text{MASnI}_3\text{-b}$ is noticeably smaller than that of $\text{MAPbI}_3\text{-b}$. Therefore a larger deviation of MA^+ from the unit-cell center in $\text{MAPbI}_3\text{-b}$ is required for $\text{H}(\text{N}) \cdots \text{I}$ bonding, as demonstrated by the fact that u_{NC} of $\text{MAPbI}_3\text{-b}$ is larger than of $\text{MASnI}_3\text{-b}$.

The X^- anions deviate from their ideal 3d Wyckoff positions as shown in Table IV. This is closely related to the $\text{H}(\text{N}) \cdots \text{X}$ hydrogen bonding. Because of the primitive-cell model and the reflectional symmetry with respect to the (020)

Table IV. Fractional coordinates of the carbon and nitrogen atoms as well as iodide anions (with the ones involved in hydrogen bonding labelled by superscript “*”) in the optimized geometries (using PBE and PBE+vdW) of the investigated hybrid perovskites in structure **b**. Lead or tin atoms are located at $(0, 0, 0)$. $\Delta(X)$ is the deviation of each halide anion from its ideal position: $(1, \frac{1}{2}, 1)$, $(1, 0, \frac{1}{2})$, $(1, 1, \frac{1}{2})$ or $(\frac{1}{2}, 1, 1)$ (note: the second and the third are equivalent because of the translational symmetry). Also listed is the u_{NC} value for each system. All data are dimensionless.

	PBE			PBE+vdW			$\Delta(X)$
	x	y	z	x	y	z	
MAPbI_3							
C	0.446	0.500	0.498	0.440	0.500	0.468	
N	0.670	0.500	0.549	0.656	0.500	0.561	
u_{NC}	3.251			2.469			
I^*	0.956	0.500	1.025	0.051	0.976	0.500	1.028
I^*	0.946	0.000	0.495	0.054	0.953	0.000	0.498
I^*	0.946	1.000	0.495	0.054	0.953	1.000	0.498
I	0.472	1.000	0.970	0.041	0.486	1.000	0.969
MASnI_3							
C	0.441	0.500	0.481	0.430	0.500	0.464	
N	0.667	0.500	0.539	0.649	0.500	0.558	
u_{NC}	2.790			2.034			
I^*	0.960	0.500	1.016	0.043	0.978	0.500	1.022
I^*	0.953	0.000	0.485	0.049	0.957	0.000	0.498
I^*	0.953	1.000	0.485	0.049	0.957	1.000	0.498
I	0.458	1.000	0.975	0.049	0.478	1.000	0.977
MAPbCl_3							
C	0.429	0.500	0.476	0.413	0.500	0.459	
N	0.674	0.500	0.550	0.654	0.500	0.556	
u_{NC}	2.404			1.698			
Cl^*	0.954	0.500	1.026	0.053	0.959	0.500	1.025
Cl^*	0.949	0.000	0.492	0.052	0.944	0.000	0.495
Cl^*	0.949	1.000	0.492	0.052	0.944	1.000	0.495
Cl	0.481	1.000	0.963	0.042	0.491	1.000	0.962

plane, this deviation is limited to the xz plane. Different to structure **a** where all halide anions equally participate in the hydrogen bonding, the three halides in the unit cell of structure **b** play different roles when interacting with the $-\text{NH}_3^+$ group. Specifically, the X^- anion approximately located at $(1, \frac{1}{2}, 1)$ (the first X^* in each block of Table IV, which is located in the (020) plane) forms a hydrogen bond with one hydrogen of the $-\text{NH}_3^+$ group. In PBE geometries, this halide anion is significantly “pulled” toward the MA^+ cation along x , and “pushed” away from the MA^+ cation along z (that is, the z -coordinate is larger than one). The deviation along x is larger than along z by a factor of ~ 2 . For both $\text{MAPbI}_3\text{-b}$ and $\text{MASnI}_3\text{-b}$, the inclusion of TS-vdW reduces its x -deviation by a factor of ~ 2 , and slightly enlarges the z -deviation. This is an accumulative result of the u_{NC} -decrease and the reduced $\Delta x : \Delta z(\text{C–N})$ ratio: they cause a decrease of the x -coordinate together with

an increase of z of the nitrogen's position, and accordingly a movement of this halide's position.

Two X^- anions, which are approximately located at $(1, 0, \frac{1}{2})$ and $(1, 1, \frac{1}{2})$, and therefore are equivalent to each other, form hydrogen bonds with the other two hydrogen atoms at the nitrogen-end. Each of them simultaneously forms two hydrogen bonds with MA^+ cations in neighbouring unit cells because of the periodic boundary condition. Table IV shows that, the deviation of these halides' positions from the 3d Wyckoff positions along x is much larger than that along z , and the effect of TS-vdW on their positions is rather small. Besides, the X^- anion approximately located at $(\frac{1}{2}, 1, 1)$ or equivalent positions (the one without the superscript-label “**” in Table IV) does not participate in hydrogen bonding. Nevertheless, its deviation along z is significantly larger than each of the other two halide anions, and this deviation is nearly unaffected by the inclusion of TS-vdW. In addition, TS-vdW reduces its deviation along x by a factor of ~ 2 . Moreover, the impact of TS-vdW on the the positions of the chloride anions in $MAPbCl_3$ is much smaller than that for both iodide-based hybrid compounds, which agrees with the fact that the vdW interactions cause the smallest change of $\Delta x : \Delta z(C-N)$ in this system.

From the PBE+vdW results of structure **b**, we observe a positive correlation between the $\Delta x/\Delta z(C-N)$ -increase and the increase of the $\Delta(X)$ -range from $MASnI_3$, $MAPbI_3$ to $MAPbCl_3$. A graphical representation is given in Fig. 5.

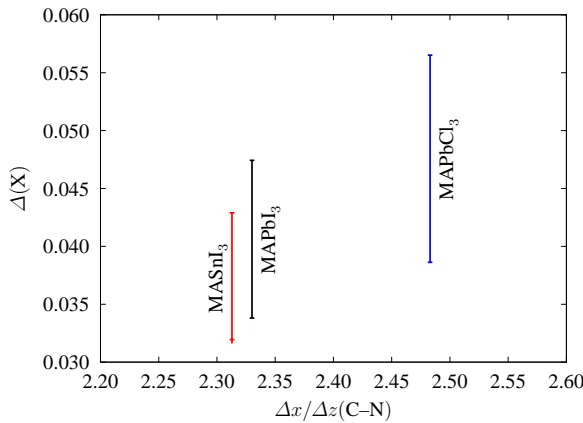


Figure 5. PBE+vdW results of $\Delta x/\Delta z(C-N)$ and the $\Delta(X)$ -range for $MAPbI_3$ -**b** (black), $MASnI_3$ -**b** (red) and $MAPbCl_3$ -**b** (blue).

C. The deformation of the inorganic framework and its interplay with the organic cation — a chicken-and-egg paradox

Next we analyse the atomic structure in more detail to decipher the interplay between the organic cation and the inorganic-framework. We will also investigate the role of vdW interactions in this interplay.

The $\Delta(X)$ values in Tables III and IV allow us to compare the inorganic-framework deformation between structures **a** and **b**. For both $MAPbI_3$ and $MAPbCl_3$ calculated with

PBE, the PbX_3^{2-} -deformation in structure **b** is larger than in structure **a** by a factor of ~ 2 , while for $MASnI_3$ the SnI_3^{2-} -deformation in **b** is only slightly larger than in **a**. The inclusion of TS-vdW in the PBE calculations causes a $\sim 60\%$ reduction of $\Delta(I)$ in both $MAPbI_3$ -**a** and $MASnI_3$ -**a**, and a less than 25% reduction in the corresponding **b** structures. As a result, the PbI_3^{2-} -deformation in the PBE+vdW structure of $MAPbI_3$ -**b** is larger than in $MAPbI_3$ -**a** by a factor of ~ 4 (this is intuitively reflected by the much more pronounced $Pb-I-Pb$ bending in Fig. 2b vs. Fig. 2a), while the SnI_3^{2-} -deformation in the PBE+vdW structure of $MASnI_3$ -**b** is larger than in $MASnI_3$ -**a** by a factor of ~ 2 . The inclusion of vdW interactions causes a $\sim 20\%$ reduction of $\Delta(Cl)$ in $MAPbCl_3$ -**a**, while the impact on $MAPbCl_3$ -**b** is weak on average.

The trend of the BX_3^{2-} -deformation qualitatively agrees with the trend of the cohesive-energy difference (ΔE_{total}) listed in Table II. For example, in PBE, the cohesive-energy difference between $MASnI_3$ -**a** and **b** is very small (3.3 meV), corresponding to the similar magnitude of the SnI_3^{2-} -deformation in these two structures. In contrast, the cohesive-energy difference in PBE+vdW becomes larger by one order of magnitude (21.6 meV), corresponding to the apparently larger SnI_3^{2-} -deformation in $MASnI_3$ -**b** than in **a**.

For a systematic analysis, we carried out PBE and PBE+vdW calculations for three models of $MAPbI_3$ -**a** and **b**. Our aim is to disentangle the direct effect of the vdW interactions from the indirect effect they have on the lattice constant. We start from an ideal PbI_3^{2-} -framework in model I, that is, no inorganic-framework deformations. We evaluate model I at both the PBE and the PBE+vdW lattice constants. Then in model II, we let the atomic positions relax in PBE at these two fixed lattice constants. Model II thus measures the effect of the distortion of the inorganic framework for the two different molecular orientations **a** and **b** as well as the effect of the lattice constant. In model III we then switch on the vdW interactions at the two lattice constants and relax the structures again. This model measures the effect of the vdW interactions at fixed lattice constant. Figure 6 reports the structural-parameters and (PBE+vdW) total-energies for the three models (we do not report the PBE total energies to simplify our discussions).

Figures 6a and b reveal that the inorganic-framework deformation has the largest effect. Going from model I to II decreases the total energy (and thus increases the stability) while simultaneously $\Delta(I)$ increases, that is, the inorganic framework deforms. This effect is more pronounced for structure **b**. This effect is fairly insensitive to the lattice constant.

Figures 6a and b further reveal that direct vdW effects are small. Going from model II to III only results in a minute energy gain (or even increase at the PBE lattice constant). The corresponding inorganic-framework distortion reduces slightly, manifested in a decrease of $\Delta(I)$. This is due to the smaller $Pb-I$ distances in PBE+vdW.

Figures 6c and d illustrate how the lattice constant, the PbI_3^{2-} -deformation and vdW interactions influence the position of MA^+ . u_{NC} is very sensitive to $\Delta(I)$: as $\Delta(I)$ increases from I, III to II, u_{NC} decreases, indicating that the MA^+ cation moves closer to the unit-cell center. These findings agree

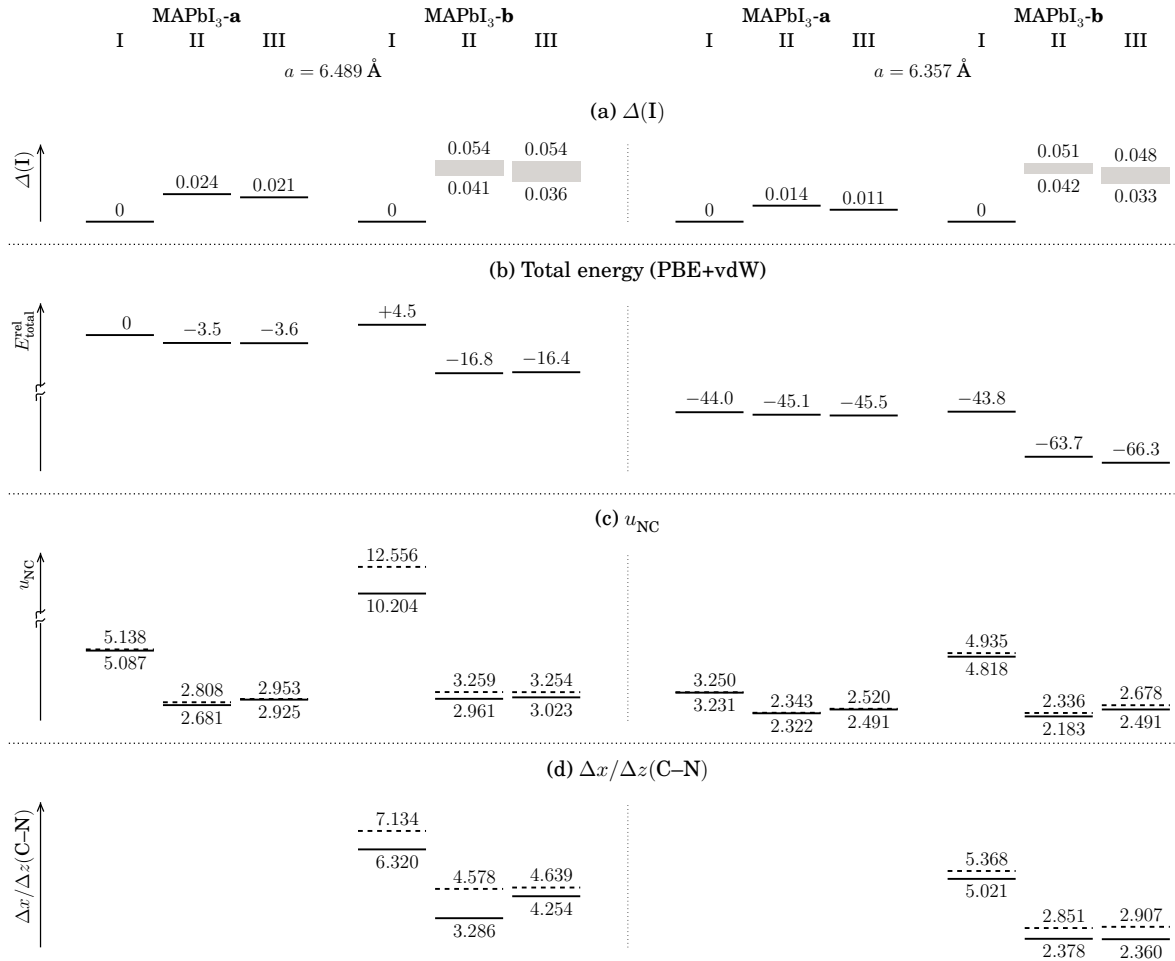


Figure 6. DFT results of MAPbI₃-**a** and **b** in models I, II and III. Shown are: (a) the $\Delta(I)$ values (or ranges for **b**-II and **b**-III) which define the models, (b) the PBE+vdW total energies, (c) u_{NC} , and (d) $\Delta x/\Delta z(C-N)$ for structure **b**. Results calculated at both PBE and PBE+vdW lattice constants (6.489 and 6.357 Å, respectively) are shown. In (c) and (d), PBE and PBE+vdW results are given in dashed and solid lines, respectively.

with those of Fig. 4, where we also observed an inverse relation between $\Delta(I)$ and u_{NC} for different hybrid perovskites. Moreover, the impact of vdW interactions on u_{NC} is generally very small. Similar trends are found for structure **b** (Fig. 6d): When the PbI₆²⁻-deformation is switched on by going from model I to II, $\Delta x/\Delta z(C-N)$ significantly decreases, indicating a larger angle between the C–N bond and the [100] direction. The effects of vdW interactions are again not large.

Recapitulating: a larger deformation of the inorganic framework corresponds to a lower total energy in MAPbI₃. A reasonable hypothesis is that the deformation of the inorganic BX₃²⁻-framework of hybrid perovskites is energetically favorable. Structure **b** is noticeably more stable, because our PBE+vdW results indicate that the orientation of the organic MA⁺ cation allows for a larger BX₃²⁻-deformation.

Can we then postulate that the BX₃²⁻-deformation intrinsically exists to stabilize the trihalide perovskites? We have carried out test calculations (PBE+vdW) for the reference compound CsPbI₃ using different models (for example, the stress-tensor optimization of supercells). The results indicate that

the ideal cubic perovskite structure without PbI₆-deformation is the most stable, which would invalidate our postulate.

The major difference between CsPbI₃ and the MA⁺-based hybrid perovskites is the symmetry of the monovalent cation: Cs⁺ is spherical, while MA⁺ belongs to C_{3v}. Accordingly, the primitive-cell symmetry of CsPbI₃, MAPbI₃-**a** and MAPbI₃-**b** descends as O_h → C_{3v} → C_s. Our results show that the BX₃²⁻-deformation increases as the symmetry reduces. To uncover the physics behind this relation, further calculations and analysis would be required. However, the trend is supported by a recent theoretical study of a similar system, CsSnI₃⁵⁶, in which the SnI₃²⁻-deformation is closely related to the phonon modes. The motion of the phonon can introduce an instantaneous symmetry break-down. However, the phonon motion is temperature-dependent and its modelling would go beyond the DFT methods employed in this article.

To summarize, the organic and the inorganic components of hybrid perovskites act synergetically: The low symmetry of the organic cation (the *chicken*) triggers the inorganic-framework (the *egg*) deformation, whose magnitude is sen-

Table V. Dependence of DFT results for MAPbI_3 (MA^+ -location, lattice constant, PbI_3^{2-} -deformation and PBE+vdW total energy) on the MA^+ -orientation, computational environments (lattice constant and PbI_3^{2-} -deformation) and DFT method (vdW interactions).

DFT results	MA^+ -orientation	lattice constant	PbI_3^{2-} -deformation	vdW interactions
MA^+ -location	–	strong	strong	weak
lattice constant	weak	–	weak	strong
PbI_3^{2-} -deformation	strong	moderate	–	moderate
PBE+vdW total energy	weak	strong	strong	–

sitive to the orientation of the organic cation; this deformation then aids the overall stabilization of the hybrid perovskite structure. The final location of the organic cation depends sensitively on the inorganic-framework deformation. We are thus left with a chicken-and-egg paradox that makes it hard to say which came first, the deformation of the inorganic-framework or position of the organic cation.

Table V sums up how the DFT total energy and structural parameters of MAPbI_3 depend on different factors. Only *direct* dependences are listed. For example, the location of MA^+ (u_{NC} and/or $\Delta x/\Delta z(\text{C-N})$) sensitively depends on the lattice constant, which is significantly reduced by vdW interactions. However, when all other factors (lattice constant and the PbI_3^{2-} -deformation) are fixed, vdW interactions have only a very weak effect on the location of MA^+ .

D. Impact of vdW interactions on the lattice constants

Our analysis of the hybrid-perovskite geometries have revealed the importance of incorporating vdW interactions into DFT calculations. The impact of vdW interactions is mainly *indirect*, as the change of the atomic structure is mainly correlated with the unit-cell volume. Next we analyse which component of the hybrid perovskites has the largest influence on the lattice constants. The TS pairwise interatomic scheme implemented in FHI-aims allows us to switch individual vdW interactions between atom pairs on or off. For example, for $\text{MAPbI}_3\text{-a}$, we start from PBE reference calculations, and switch on the TS-vdW interaction selectively between different pairs, such as the MA^+ cations (denoted MA-MA), Pb-Pb, I-I, MA-Pb, MA-I, or Pb-I. For simplicity, we regard the MA^+ cation as a whole “particle”, that is, for MA-MA calculations, we switch on the TS-vdW interactions C-C, N-N, H-H, C-N, C-H, and N-H; all these interactions are switched off for other calculations, for example, MA-I. This would introduce some error, as the vdW interactions within the same MA^+ cation is considered when calculating MA-MA, but neglected for other calculations. We expect this error to be small, since the internal structure of MA^+ does not depend sensitively on the chosen DFT method as alluded to earlier.

We have performed our analysis by scanning over a certain lattice-constant range. At each lattice constant, we optimize the geometry with PBE. The total-energy corrections for the pairwise TS-vdW interactions are plotted in Fig. 7. When analysing the impact of vdW on the lattice constant, the mean-

ingful observable is not $\Delta E_{\text{total}}^{\text{TS-vdW}}$, which is defined by the total-energy difference between the PBE+vdW and the PBE calculations, but rather its gradient with respect to the lattice constant a .

Our calculations semi-quantitatively reproduce the results of Egger and Kronik³⁰ in that the vdW interaction between the iodine atoms provides the largest interatomic contribution (~ 100 meV per pair) in MAPbI_3 (Fig. 7a and b), while in MAPbCl_3 (Fig. 7d) the inter-halide interaction energy decreases by a factor of ~ 2 . However, Egger and Kronik have not summed up the interaction involving the carbon, nitrogen and hydrogen atoms, whichs play an important role in the total-energy correction as shown in Fig. 7. They have also not carried out an analysis for different lattice constants, and therefore could not determine the contribution of different pairs to the lattice constant.

Among the convex $E_{\text{total}}^{\text{PBE}}$ quasi-parabolas, the curve for $\text{MASnI}_3\text{-a}$ (Fig. 7c) is the widest, while the curve of $\text{MAPbCl}_3\text{-a}$ (Fig. 7d: only for $a < 5.85$ Å, that is, the “left half” of the curve) is the narrowest. The total-energy correction for each considered vdW pair becomes more negative for decreasing a . Hence, as expected, the inclusion of vdW interactions leads to a smaller unit-cell volume. We also observe that (i) most of the $\Delta E_{\text{total}}^{\text{TS-vdW}}$ corrections are approximately linear in a , and (ii) in different perovskites, the same pair has roughly the same effect on the lattice constant. For example, the MA-I curves for $\text{MAPbI}_3\text{-a}$ (Fig. 7a), $\text{MAPbI}_3\text{-b}$ (Fig. 7b) and $\text{MASnI}_3\text{-a}$ (Fig. 7c) agree to within 2.5 meV in the interval $a \in [6.20, 6.55]$.

For a quantitative analysis, we have performed a second-order polynomial fit (using the nonlinear least-squares Levenberg-Marquardt algorithm) to the PBE total-energy data

$$E_{\text{total}}^{\text{PBE}} = \alpha^{\text{PBE}} a^2 + \beta^{\text{PBE}} a + \gamma^{\text{PBE}} \quad (1)$$

and linear fits to the vdW total-energy corrections

$$\Delta E_{\text{total}}^{\text{TS-vdW}}(\text{Y-Z}) = \beta^{\text{TS-vdW}}(\text{Y-Z})a + \gamma^{\text{TS-vdW}}(\text{Y-Z}) \quad (2)$$

for each system, with Y-Z labelling all considered inter-particle pairs. The optimized lattice constant a^* calculated purely with PBE is given by the location of the minimum of the fitted second-order polynomial (1), while the one including the Y-Z interaction is given by the minimum-location of

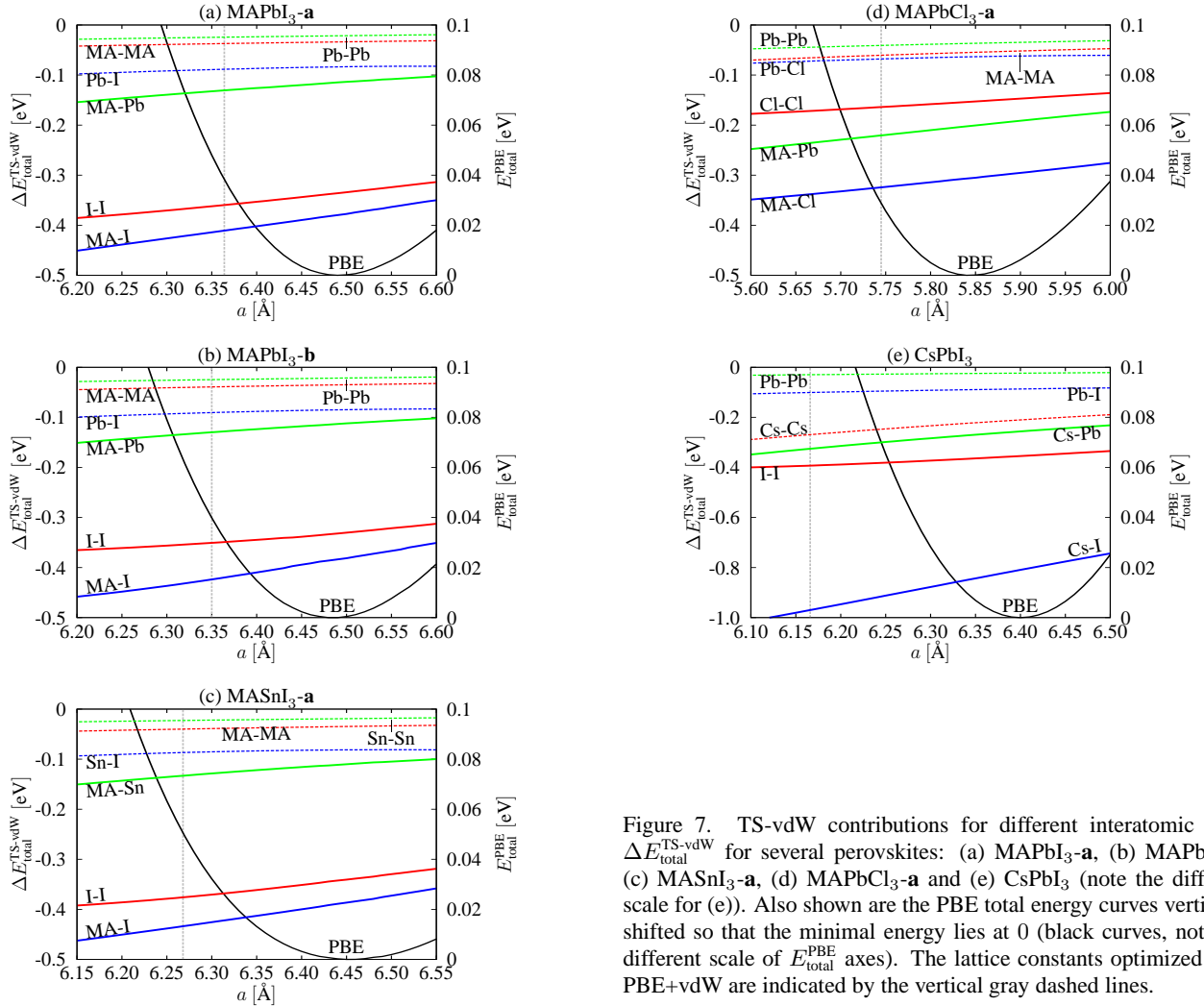


Figure 7. TS-vdW contributions for different interatomic pairs $\Delta E_{\text{total}}^{\text{TS-vdW}}$ for several perovskites: (a) $\text{MAPbI}_3\text{-a}$, (b) $\text{MAPbI}_3\text{-b}$, (c) $\text{MASnI}_3\text{-a}$, (d) $\text{MAPbCl}_3\text{-a}$ and (e) CsPbI_3 (note the different scale for (e)). Also shown are the PBE total energy curves vertically shifted so that the minimal energy lies at 0 (black curves, note the different scale of $E_{\text{total}}^{\text{PBE}}$ axes). The lattice constants optimized with PBE+vdW are indicated by the vertical gray dashed lines.

the second-order polynomial combining Eqs. (1) and (2):

$$a_{\text{PBE}}^* = -\frac{\beta^{\text{PBE}}}{2\alpha^{\text{PBE}}}, \quad (3)$$

$$a_{\text{PBE+vdW}}^*(Y-Z) = -\frac{\beta^{\text{PBE}} + \beta^{\text{TS-vdW}}(Y-Z)}{2\alpha^{\text{PBE}}}. \quad (4)$$

Table VI shows the results for $\text{MAPbI}_3\text{-b}$ and CsPbI_3 (the results for all hybrid perovskites in structure **a** are given in Table S3). We have omitted the $\Delta E_{\text{total}}^{\text{TS-vdW}}(\text{Pb-I})$ -data with $a > 6.50 \text{ \AA}$ of $\text{MAPbI}_3\text{-b}$ for a better linear fit. This is safe, as these data do not play any role in the lattice-constant reduction. For $\text{MAPbI}_3\text{-b}$, Egger and Kronik identified the I-I interaction to be most dominant³⁰. However, Fig. 7 reveals that the MA-I interaction is even larger. Furthermore, the gradient of the MA-I / MA-Pb line is steeper than / similar to the I-I line, which implies that the MA-I / MA-Pb interaction has a larger / similar influence on the lattice constant. Finally, MA-MA and Pb-Pb contribute only little (less than 1%). This might be due to the very large inter-particle distances.

Compared with $\text{MAPbI}_3\text{-b}$, CsPbI_3 exhibits a narrower PBE total-energy curve (corresponding to a larger

α^{PBE} value), as well as slightly larger gradients for $\Delta E_{\text{total}}^{\text{TS-vdW}}(\text{Pb-Pb})$, $\Delta E_{\text{total}}^{\text{TS-vdW}}(\text{I-I})$ and $\Delta E_{\text{total}}^{\text{TS-vdW}}(\text{Pb-I})$. The PbI_3^{2-} contribution to the lattice-constant reduction in these two systems is very similar. The major difference arises from the A^+ cation, as the gradients of all Cs^+ -based $\Delta E_{\text{total}}^{\text{TS-vdW}}$ lines are much larger than their MA^+ counterparts. In particular, Cs-Cs causes a lattice-constant reduction by 0.039 \AA (6.1%), while the contribution of MA-MA, as mentioned earlier, is almost negligible. The largest contribution (1.7%) comes from Cs-I. Consequently, vdW interactions in CsPbI_3 result in the largest lattice-constant reduction in all investigated systems, as shown in Table II.

In Table VI (and Table S3), we have switched on the TS-vdW interaction of each inter-particle pair separately, that is, vdW interactions of all other pairs are switched off. By summing up all contributions of the inter-particle pairs, we reach a “total correction” $\sum_{Y-Z} \Delta a_{\text{TS-vdW}}^*(Y-Z)$, and the corresponding “optimized” lattice constant $a^* = a_{\text{PBE}}^* - \sum_{Y-Z} \Delta a_{\text{TS-vdW}}^*(Y-Z)$. In general, these a^* values are quite close to the lattice constants optimized using PBE+vdW, indicating that the lattice-constant corrections from the TS-vdW

Table VI. Effects of the TS-vdW interactions for each atom or particle pair for $\text{MAPbI}_3\text{-b}$ and CsPbI_3 . For each system, we fit the second-order polynomial $E_{\text{total}}^{\text{PBE}} = \alpha^{\text{PBE}} a^2 + \beta^{\text{PBE}} a + \gamma^{\text{PBE}}$ to the total energy calculated with PBE and list α^{PBE} and β^{PBE} . We also fit the linear function $\Delta E_{\text{total}}^{\text{TS-vdW}} = \beta^{\text{TS-vdW}} a + \gamma^{\text{TS-vdW}}$ to each vdW total-energy correction. Also listed are the optimized lattice constant a^* (calculated using Eq. (3) or (4)) and its deviation Δa^* to the PBE result. For the PBE+vdW results, all listed Δa^* -deviations are summed up to a value shown in the “Sum” row.

	a^* [Å]	Δa^* [Å]	Fitting parameters
MAPbI₃-b			
PBE			α^{PBE} β^{PBE}
	6.486		2.4970 -32.392
PBE+vdW			$\beta^{\text{TS-vdW}}$
with MA-MA	6.480	-0.006 (-0.9‰)	0.031
with Pb-Pb	6.482	-0.004 (-0.7‰)	0.022
with I-I	6.460	-0.026 (-4.0‰)	0.131
with MA-Pb	6.462	-0.024 (-3.8‰)	0.122
with MA-I	6.431	-0.055 (-8.4‰)	0.273
with Pb-I	6.476	-0.010 (-1.6‰)	0.051
Sum	6.360	-0.126 (-19.4‰)	
CsPbI₃			
PBE			α^{PBE} β^{PBE}
	6.398		3.1723 -40.596
PBE+vdW			$\beta^{\text{TS-vdW}}$
with Cs-Cs	6.359	-0.039 (-6.1‰)	0.247
with Pb-Pb	6.394	-0.004 (-0.6‰)	0.026
with I-I	6.372	-0.026 (-4.1‰)	0.166
with Cs-Pb	6.352	-0.046 (-7.2‰)	0.291
with Cs-I	6.291	-0.107 (-16.8‰)	0.680
with Pb-I	6.389	-0.009 (-1.4‰)	0.059
Sum	6.167	-0.232 (-36.2‰)	

interaction of different inter-particle pairs are approximately additive⁵⁷.

These findings are instructive for the design of new hybrid perovskites toward the target unit-cell volumes, which are closely related to the materials’ electronic properties (as demonstrated by our test calculations). Comparing Fig. 7a with Fig. 7c (or the first and the second panel of Table S3), we find that the $E_{\text{total}}^{\text{PBE}}$ vs. a curve of $\text{MAPbI}_3\text{-a}$ is much narrower than that of $\text{MASnI}_3\text{-a}$. As a result, vdW interactions with similar $\beta^{\text{TS-vdW}}$ parameters (such as I-I) have less impact on the lattice constant in $\text{MAPbI}_3\text{-a}$ than they do in $\text{MASnI}_3\text{-a}$. Conversely, we have performed test calcula-

tions for $\text{CF}_3\text{NH}_3\text{PbI}_3\text{-a}$. Compared with the isostructural CH_3NH_3^+ cation, the trifluoride CF_3NH_3^+ cation is subject to stronger vdW interactions due to the larger number of electrons. TS-vdW reduces the lattice constant of $\text{CF}_3\text{NH}_3\text{PbI}_3\text{-a}$ by 0.199 Å (from 6.629 to 6.430 Å). This effect is larger than in $\text{CH}_3\text{NH}_3\text{PbI}_3\text{-a}$ (0.127 Å, see Table I). To systematically exploit this effect for materials design, however, we would need to explore hybrid perovskites with many different compositions.

IV. CONCLUSIONS

We have studied the atomic structure of a series of organometal-halide perovskites using DFT focussing in particular on the interaction between the organic cation and the inorganic matrix. We identify two stable configurations of the organic cation and analyse the associated deformation of the inorganic-framework in detail. The incorporation of vdW interactions into semi-local DFT calculations significantly corrects the calculated lattice constants and thus indirectly but strongly affects the atomic structure of hybrid perovskites. We further analyse the individual vdW contributions and identified the MA-I, I-I and MA-Pb interactions with the largest effect on the lattice constants. Our analysis of the vdW contributions provides insight into the design of new hybrid perovskites with favorable structural properties. This work serves as a foundation for future studies aiming at a supercell description of hybrid perovskites that reveals the tilting of the metal-halide octahedra and the alignment of organic cations in these systems as well as their mutual interplay.

ACKNOWLEDGMENT

We thank H. Levard, M. Puska and K. Laasonen as well as A. Tkatchenko, V. Blum and A. Gulans for fruitful discussions. The generous allocation of computing resources by the CSC-IT Center for Science (via the Project No. ay6311) and the Aalto Science-IT project are gratefully acknowledged. This work was supported by the Academy of Finland through its Centres of Excellence Programme (2012-2014 and 2015-2017) under project numbers 251748 and 284621.

ASSOCIATED CONTENT

Supplemental Material: TS-vdW parameters for each atom; full coordinates of the investigated systems; vdW-caused lattice-constant corrections for $\text{MAPbI}_3\text{-a}$, $\text{MASnI}_3\text{-a}$ and $\text{MAPbCl}_3\text{-a}$. This material is available free of charge via the internet at <http://journals.aps.org>.

* jingrui.li@aalto.fi

¹ H. J. Snaith, J. Phys. Chem. Lett. **4**, 3623 (2013).

² M. A. Green, A. Ho-Baillie, and H. J. Snaith, Nature Photon. **8**, 506 (2014).

³ http://www.nrel.gov/ncpv/images/efficiency_chart.jpg (National Renewable Energy Laboratory: Best research-cell efficiencies, 2015).

⁴ A. Kojima, K. Teshima, Y. Shirai, and T. Miyasaka, *J. Am. Chem. Soc.* **131**, 6050 (2009).

⁵ H.-S. Kim, C.-R. Lee, J.-H. Im, K.-B. Lee, T. Moehl, A. Marchioro, S.-J. Moon, R. Humphry-Baker, J.-H. Yum, J. E. Moser, et al., *Sci. Rep.* **2**, 591 (2012).

⁶ M. M. Lee, J. Teuscher, T. Miyasaka, T. N. Murakami, and H. J. Snaith, *Science* **338**, 643 (2012).

⁷ N.-J. Jeon, J. H. Noh, W.-S. Yang, Y.-C. Kim, S.-C. Ryu, J.-W. Seo, and S.-I. Seok, *Nature* **517**, 476 (2015).

⁸ W. Shockley and H.-J. Queisser, *J. Appl. Phys.* **32**, 510 (1961).

⁹ S. de Wolf, J. Holovsky, S.-J. Moon, P. Löper, B. Niesen, M. Ledinsky, F.-J. Haug, J.-H. Yum, and C. Ballif, *J. Phys. Chem. Lett.* **5**, 1035 (2014).

¹⁰ S. D. Stranks, G. E. Eperon, G. Grancini, C. Menelaou, M. J. P. Alcocer, T. Leijtens, L. M. Herz, A. Petrozza, and H. J. Snaith, *Science* **342**, 341 (2013).

¹¹ G. Xing, N. Mathews, S. Sun, S. S. Lim, Y. M. Lam, M. Grätzel, S. Mhaisalkar, and T. C. Sum, *Science* **342**, 344 (2013).

¹² E. Mosconi, A. Amat, M. K. Nazeeruddin, M. Grätzel, and F. de angelis, *J. Phys.: Condens. Matter* **117**, 13902 (2013).

¹³ F. Brivio, A. B. Walker, and A. Walsh, *APL Mater.* **1**, 042111 (2013).

¹⁴ A. Filippetti and A. Mattoni, *Phys. Rev. B* **89**, 125203 (2014).

¹⁵ I. E. Castelli, J. M. García-Lastra, K. S. Thygesen, and K. W. Jacobsen, *APL Mater.* **2**, 081514 (2014).

¹⁶ W. Yin, J. Yang, J.-G. Kang, Y. Yan, and S. Wei, *J. Mater. Chem. A* **3**, 8926 (2015).

¹⁷ I. Borriello, G. Cantele, and D. Ninno, *Phys. Rev. B* **77**, 235214 (2008).

¹⁸ A. Amat, E. Mosconi, E. Ronca, C. Quarti, P. Umari, M. K. Nazeeruddin, M. Grätzel, and F. de Angelis, *Nano Lett.* **14**, 3608 (2014).

¹⁹ E. Mosconi, C. Quarti, T. Ivanovska, G. Ruani, and F. de Angelis, *Phys. Chem. Chem. Phys.* **16**, 16137 (2014).

²⁰ L. Y. Huang and W. R. L. Lambrecht, *Phys. Rev. B* **90**, 195201 (2014).

²¹ J. Even, L. Pedesseau, M.-A. Dupertuis, J.-M. Jancu, and C. Katan, *Phys. Rev. B* **86**, 205301 (2012).

²² J. Even, L. Pedesseau, J.-M. Jancu, and C. Katan, *J. Phys. Chem. Lett.* **4**, 2999 (2013).

²³ F. Brivio, K. T. Butler, A. Walsh, and M. van Schilfgaarde, *Phys. Rev. B* **89**, 155204 (2014).

²⁴ C. Katan, L. Pedesseau, M. Kepenekian, A. Rolland, and J. Even, *J. Mater. Chem. A* **3**, 9232 (2015).

²⁵ P. Umari, E. Mosconi, and F. de Angelis, *Sci. Rep.* **4**, 4467 (2014).

²⁶ T. Ahmed, C. L. o vorakiat, T. Salim, Y. M. Lam, E. E. M. Chia, and J. Zhu, *Europhys. Lett.* **108**, 67015 (2014).

²⁷ J. M. Frost, K. T. Butler, F. Brivio, C. H. Hendon, M. van Schilfgaarde, and A. Walsh, *Nano Lett.* **14**, 2584 (2014).

²⁸ J. M. Frost, K. T. Butler, and A. Walsh, *APL Mater.* **2**, 081506 (2014).

²⁹ A. M. A. Leguy, J. M. Frost, A. P. McMahon, V. Garcia Sakai, W. Kochelmann, C. H. Law, X. Li, F. Foglia, A. Walsh, B. C. O'Regan, et al., *Nature Comm.* **6**, 7124 (2015).

³⁰ D. A. Egger and L. Kronik, *J. Phys. Chem. Lett.* **5**, 2728 (2014).

³¹ C. Motta, F. El-Mellouhi, S. Kais, N. Tabet, F. Alharbi, and S. Sanvito, *Nature Comm.* **6**, 7026 (2015).

³² Y. Wang, T. Gould, J. F. Dobson, H. Zhang, H. Yang, X. Yao, and H. Zhao, *Phys. Chem. Chem. Phys.* **16**, 1424 (2014).

³³ A. Tkatchenko and M. Scheffler, *Phys. Rev. Lett.* **102**, 073005 (2009).

³⁴ J. P. Perdew, K. Burke, and M. Ernzerhof, *Phys. Rev. Lett.* **77**, 3865 (1996).

³⁵ E. van Lenthe, E. J. Baerends, and J. G. Sneijders, *J. Chem. Phys.* **99**, 4597 (1993).

³⁶ G. X. Zhang, A. Tkatchenko, J. Paier, H. Appel, and M. Scheffler, *Phys. Rev. Lett.* **107**, 245501 (2011).

³⁷ T. Bučko, S. Lebègue, J. Hafner, and J. Ángyán, *J. Chem. Theo. Comput.* **9**, 4293 (2013).

³⁸ T. Bučko, S. Lebègue, J. Ángyán, and J. Hafner, *J. Chem. Phys.* **131**, 034114 (2014).

³⁹ V. Blum, R. Gehrke, F. Hanke, P. Havu, V. Havu, X. Ren, K. Reuter, and M. Scheffler, *Comput. Phys. Comm.* **180**, 2175 (2009).

⁴⁰ V. Havu, V. Blum, P. Havu, and M. Scheffler, *J. Comput. Phys.* **228**, 8367 (2009).

⁴¹ S. V. Levchenko, X. Ren, J. Wieferink, R. Johanni, P. Rinke, V. Blum, and M. Scheffler, *Comput. Phys. Comm.* **192**, 60 (2015), ISSN 0010-4655.

⁴² C. C. Stoumpos, C. D. Malliakas, and M. G. Kanatzidis, *Inorg. Chem.* **52**, 9019 (2013).

⁴³ A. Poglitsch and D. Weber, *J. Chem. Phys.* **87**, 6373 (1987).

⁴⁴ L. Chi, I. Swainson, L. Cranswick, J.-H. Her, P. Stephens, and O. Knop, *J. Solid State Chem.* **178**, 1376 (2005).

⁴⁵ G. E. Eperon, G. M. Paternò, R. J. Sutton, A. Zampetti, A. A. Haghhighirad, F. Cacialli, and H. Snaith, *J. Mater. Chem. A* **3**, 19688 (2015).

⁴⁶ F. Knuth, C. Carbogno, V. Atalla, V. Blum, and M. Scheffler, *Comput. Phys. Comm.* **190**, 33 (2015).

⁴⁷ H. Levard, private communication.

⁴⁸ M. T. Weller, O. J. Weber, P. F. Henry, A. M. di Pumbo, and T. C. Hansen, *Chem. Commun.* **51**, 4180 (2015).

⁴⁹ R. S. Seymour and A. W. Pryor, *Acta Crystallogr. B* **26**, 1487 (1970).

⁵⁰ H. A. Levy and S. W. Peterson, *Phys. Rev.* **86**, 766 (1952).

⁵¹ J. Ireta, J. Neugebauer, and M. Scheffler, *J. Phys. Chem. A* **108**, 5692 (2004).

⁵² N. Marom, A. Tkatchenko, M. Rossi, V. V. Gobre, O. Hod, M. Scheffler, and L. Kronik, *J. Chem. Theo. Comput.* **7**, 3944 (2011).

⁵³ L. Kronik and A. Tkatchenko, *Acc. Chem. Res.* **47**, 3208 (2014).

⁵⁴ Z. Cheng and J. Lin, *CrystEngComm* **12**, 2246 (2010).

⁵⁵ T. Baikie, Y. Fang, J. M. Kadro, M. Schreyer, F. Wei, S. G. Mhaisalkar, M. Grätzel, and T. J. White, *J. Mater. Chem. A* **1**, 5628 (2013).

⁵⁶ C. E. Patrick, K. W. Jacobsen, and K. S. Thygesen, *Phys. Rev. B* **92**, 201205(R) (2015).

⁵⁷ For CsPbI_3 there is nearly no difference between this a^* value and the PBE+vdW lattice constant, while for each hybrid perovskite, the former is slightly larger. This is because of the pairwise and additive character of the TS method, as well as the fact that TS-vdW does not relax the PBE geometry of CsPbI_3 at each lattice constant. However, the latter factor is not valid for hybrid perovskites, since the outlined calculations are based on the PBE geometry at each lattice constant, which is different to the PBE+vdW geometry. For a comparison we can recall Figs. 6a, c and d: TS-vdW results in smaller PbI_3^{2-} -deformation which sensitively affects the structural parameters of MA^+ . These geometrical deviations are the major source of the discrepancy between the a^* obtained from the “total-correction” approach and the PBE+vdW lattice constant. Another source would be the quality of fitting, such as the anharmonicity of $E_{\text{total}}^{\text{PBE}}$ and the nonlinearity of $\Delta E_{\text{total}}^{\text{TS-vdW}}$ with respect to a .

Supplemental Material

Table S1. TS-vdW parameters (density-scaled atomic polarizability α , C_6 coefficient and vdW radius R_0) for each atom considered in this work. All data are in atomic units.

	α	C_6	R_0
H	4.50	6.500	3.100
C	12.00	46.600	3.590
N	7.40	24.200	3.340
Cl	15.00	94.600	3.710
Sn	55.95	587.417	4.303
I	35.00	385.000	4.170
Cs	427.12	6582.080	3.780
Pb	61.80	697.000	4.310

Table S2. Fractional coordinates of all inequivalent nuclei in optimized cubic primitive cells of all investigated hybrid perovskites: MAPbI_3 -**a/b**, MASnI_3 -**a/b**, and MAPbCl_3 -**a/b**. Both results calculated with PBE and PBE+vdW are listed.

	PBE			PBE+vdW			PBE			PBE+vdW		
	x	y	z	x	y	z	x	y	z	x	y	z
MAPbI_3-a												
C	0.464	0.464	0.464	0.462	0.462	0.462	0.446	0.500	0.498	0.440	0.500	0.468
H	0.367	0.563	0.367	0.364	0.563	0.364	0.376	0.361	0.565	0.357	0.359	0.521
H	0.367	0.367	0.563	0.364	0.364	0.563	0.428	0.500	0.331	0.454	0.500	0.297
H	0.563	0.367	0.367	0.563	0.364	0.364	0.376	0.638	0.565	0.357	0.641	0.521
N	0.596	0.596	0.596	0.597	0.597	0.597	0.670	0.500	0.549	0.656	0.500	0.561
H	0.693	0.512	0.693	0.696	0.512	0.696	0.744	0.630	0.491	0.741	0.632	0.516
H	0.693	0.693	0.512	0.696	0.696	0.512	0.698	0.500	0.707	0.656	0.500	0.724
H	0.512	0.693	0.693	0.512	0.696	0.696	0.744	0.370	0.491	0.741	0.368	0.516
Pb	0.000	0.000	0.000	0.000	0.000	0.000	0.000	0.000	0.000	0.000	0.000	0.000
I	-0.016	0.487	-0.016	-0.006	0.496	-0.007	-0.044	0.500	0.025	-0.024	0.500	0.028
I	-0.016	-0.016	0.487	-0.007	-0.006	0.496	-0.054	0.000	0.495	-0.047	0.000	0.498
I	0.487	-0.016	-0.016	0.496	-0.007	-0.006	0.472	0.000	-0.030	0.486	0.000	-0.031
MASnI_3-a												
C	0.461	0.461	0.461	0.452	0.452	0.452	0.441	0.500	0.481	0.430	0.500	0.464
H	0.364	0.560	0.364	0.352	0.555	0.352	0.369	0.360	0.546	0.346	0.356	0.517
H	0.364	0.364	0.560	0.352	0.352	0.554	0.429	0.500	0.311	0.445	0.500	0.290
H	0.560	0.364	0.364	0.554	0.352	0.352	0.369	0.640	0.546	0.346	0.644	0.517
N	0.594	0.594	0.594	0.589	0.589	0.589	0.667	0.500	0.539	0.649	0.500	0.558
H	0.691	0.509	0.691	0.689	0.502	0.689	0.744	0.631	0.482	0.736	0.634	0.513
H	0.691	0.691	0.509	0.689	0.689	0.502	0.691	0.500	0.700	0.648	0.500	0.724
H	0.509	0.691	0.691	0.502	0.689	0.689	0.744	0.369	0.482	0.736	0.366	0.513
Sn	0.000	0.000	0.000	0.000	0.000	0.000	0.000	0.000	0.000	0.000	0.000	0.000
I	-0.019	0.466	-0.019	-0.009	0.489	-0.009	-0.040	0.500	0.016	-0.022	0.500	0.022
I	-0.019	-0.019	0.466	-0.009	-0.009	0.489	-0.047	0.000	0.485	-0.043	0.000	0.498
I	0.466	-0.019	-0.019	0.489	-0.009	-0.009	0.458	0.000	-0.025	0.478	0.000	-0.023
MAPbCl_3-a												
C	0.452	0.452	0.452	0.443	0.443	0.443	0.429	0.500	0.476	0.413	0.500	0.459
H	0.344	0.561	0.344	0.333	0.554	0.333	0.346	0.345	0.543	0.322	0.343	0.519
H	0.344	0.344	0.561	0.333	0.333	0.554	0.423	0.500	0.288	0.424	0.500	0.268
H	0.561	0.344	0.344	0.554	0.333	0.333	0.346	0.655	0.543	0.322	0.657	0.519
N	0.598	0.598	0.598	0.592	0.592	0.592	0.674	0.500	0.550	0.654	0.500	0.556
H	0.706	0.506	0.706	0.701	0.498	0.701	0.760	0.645	0.491	0.747	0.647	0.504
H	0.706	0.706	0.506	0.701	0.701	0.498	0.693	0.500	0.728	0.659	0.500	0.737
H	0.506	0.706	0.706	0.498	0.701	0.701	0.760	0.355	0.491	0.747	0.353	0.504
Pb	0.000	0.000	0.000	0.000	0.000	0.000	0.000	0.000	0.000	0.000	0.000	0.000
Cl	-0.019	0.484	-0.019	-0.018	0.492	-0.018	-0.046	0.500	0.026	-0.041	0.500	0.025
Cl	-0.019	-0.019	0.484	-0.018	-0.018	0.492	-0.051	0.000	0.492	-0.056	0.000	0.495
Cl	0.484	-0.019	-0.019	0.492	-0.018	-0.018	0.481	0.000	-0.037	0.491	0.000	-0.038

Table S3. Effects of the TS-vdW interactions for each particle pair for **MAPbI₃-a**, **MASnI₃-a** and **MAPbCl₃-a**. For each system, we fit the second-order polynomial $E_{\text{total}}^{\text{PBE}} = \alpha^{\text{PBE}} a^2 + \beta^{\text{PBE}} a + \gamma^{\text{PBE}}$ to the total energy calculated with PBE and list α^{PBE} and β^{PBE} . We also fit the linear function $\Delta E_{\text{total}}^{\text{TS-vdW}} = \beta^{\text{TS-vdW}} a + \gamma^{\text{TS-vdW}}$ to each vdW total-energy correction. Also listed are the optimized lattice constant a^* calculated for each pair and its deviation Δa^* to the PBE result. For the PBE+vdW results, all listed Δa^* -deviations are summed up to a value shown in the “Sum” row.

	$a^* \text{ [\AA]}$	$\Delta a^* \text{ [\AA]}$	Fitting parameters	
MAPbI₃-a				
PBE			α^{PBE}	β^{PBE}
	6.493		2.7247	-35.382
PBE+vdW			$\beta^{\text{TS-vdW}}$	
with MA-MA	6.488	-0.005 (-0.8‰)		0.027
with Pb-Pb	6.489	-0.004 (-0.6‰)		0.023
with I-I	6.460	-0.033 (-5.1‰)		0.181
with MA-Pb	6.469	-0.024 (-3.6‰)		0.128
with MA-I	6.447	-0.046 (-7.1‰)		0.250
with Pb-I	6.484	-0.009 (-1.4‰)		0.049
Sum	6.372	-0.121(-18.6‰)		
MASnI₃-a				
PBE			α^{PBE}	β^{PBE}
	6.445		1.9335	-24.921
PBE+vdW			$\beta^{\text{TS-vdW}}$	
with MA-MA	6.437	-0.007 (-1.2‰)		0.029
with Sn-Sn	6.440	-0.005 (-0.8‰)		0.020
with I-I	6.396	-0.048 (-7.5‰)		0.187
with MA-Sn	6.412	-0.033 (-5.1‰)		0.127
with MA-I	6.378	-0.067(-10.4‰)		0.260
with Sn-I	6.434	-0.011 (-1.7‰)		0.042
Sum	6.273	-0.172(-26.7‰)		
MAPbCl₃-a				
PBE*			α^{PBE}	β^{PBE}
	5.845		3.5074	-40.998
PBE+vdW			$\beta^{\text{TS-vdW}}$	
with MA-MA	5.836	-0.008 (-1.4‰)		0.057
with Pb-Pb	5.839	-0.006 (-1.0‰)		0.041
with Cl-Cl	5.829	-0.015 (-2.6‰)		0.106
with MA-Pb	5.818	-0.027 (-4.6‰)		0.187
with MA-Cl	5.818	-0.026 (-4.5‰)		0.183
with Pb-Cl	5.837	-0.007 (-1.2‰)		0.051
Sum	5.755	-0.089(-15.3‰)		

